

SPACE-TIME UNFITTED FINITE ELEMENTS ON MOVING EXPLICIT GEOMETRY REPRESENTATIONS

SANTIAGO BADIA^{1,2}, PERE A. MARTORELL^{3,*}, AND FRANCESC VERDUGO⁴

ABSTRACT. This work proposes a novel variational approximation of partial differential equations on moving geometries determined by explicit boundary representations. The benefits of the proposed formulation are the ability to handle large displacements of explicitly represented domain boundaries without generating body-fitted meshes and remeshing techniques. For the space discretization, we use a background mesh and an unfitted method that relies on the integration on cut cells. We perform this intersection by using clipping algorithms. To deal with the mesh movement, we pullback the equations to a reference configuration (the spatial mesh at the initial time slab times the time interval) that is constant in time. This way, the geometrical intersection algorithm is only required in 3D, another key property of the proposed scheme. At the end of the time slab, we compute the deformed mesh, intersect the deformed boundary with the background mesh, and consider an exact transfer mechanism between meshes to compute jump terms in the time discontinuous Galerkin integration. The transfer is also computed using geometrical intersection algorithms. We demonstrate the applicability of the method to fluid problems around rotating (2D and 3D) geometries described by oriented boundary meshes. We also provide a set of numerical experiments that show the optimal convergence of the method.

Keywords: Unfitted finite elements, embedded finite elements, computer-aided design, computational geometry, immersed boundaries, boundary representations, space-time discretizations, large displacements.

1. INTRODUCTION

Space-time formulations for finite element methods (FEMs) are valuable techniques for solving transient numerical problems. Unlike standard time stepping schemes, which employ different discretizations for space and time, space-time formulations discretize the problem simultaneously in both space and time. However, generating 4D space-time body-fitted meshes becomes extremely challenging on moving complex geometries. There are no general-purpose tools to generate 4D meshes. Besides, the re-meshing process due to moving domains introduces projection errors when transferring between meshes.

The bottleneck of mesh generation can be addressed by employing unfitted FEMs. Unfitted FEMs, also known as embedded or immersed FEMs, offer a solution that eliminates the need for body-fitted mesh generation, relying instead on a simple background grid, such as a uniform or adaptive Cartesian grid. For large-scale simulations on distributed-memory platforms, one can replace expensive (both in terms of computational time and memory) unstructured mesh partitioning [1] by efficient tree-mesh partitioners with load balancing [2, 3]. Unfitted FEMs have

¹ School of Mathematics, Monash University, Clayton, Victoria, 3800, Australia.

² Centre Internacional de Mètodes Numèrics a l'Enginyeria, Campus Nord, 08034, Barcelona, Spain.

³ Department of Civil and Environmental Engineering, Universitat Politècnica de Catalunya, Edifici C1, Campus Nord UPC, Jordi Girona 1-3, 08034 Barcelona, Spain.

⁴ Department of Computer Science, Vrije Universiteit Amsterdam, De Boelelaan 1111, 1081 HV Amsterdam, The Netherlands.

* Corresponding author.

E-mails: santiago.badia@monash.edu (SB), pere.antoni.martorell@upc.edu (PM), f.verdugo.rojano@vu.nl (FV).

gained increasing popularity in various applications, including fluid-structure interaction (FSI) [4, 5, 6], fracture mechanics [7, 8], additive manufacturing [9, 10], and stochastic geometry problems [11]. Traditionally, unfitted problems utilize level sets to describe geometries. However, recent work [12, 13] has extended unfitted discretizations to simulate geometries described by computer-aided design (CAD) models, i.e., explicit geometry representations.

The small cut cell problem, commonly discussed in the literature [14], is a significant limitation of unfitted FEMs. The intersection between the physical domain and the background cells can become arbitrarily small, thereby giving rise to ill-conditioning issues. While several authors have attempted to address this problem, only a few techniques have demonstrated robustness and optimal convergence. The ghost penalty methods [15], employed within the so-called CutFEM framework [16], represent one such approach. Alternatively, cell agglomeration techniques have emerged as viable options to ensure robustness in the presence of cut cells, naturally applied on discontinuous Galerkin (DG) methods [17]. Extensions to the C^0 Lagrangian finite element (FE) have been introduced in [18], while mixed methods have been explored in [19], where the aggregated finite element method (AgFEM) term was coined. AgFEM exhibits good numerical qualities, including stability, bounds on condition numbers, optimal convergence, and continuity concerning data. Distributed implementations have been exploited in [20, 21], while AgFEM has also been extended to h -adaptive meshes [22] and higher-order FE [23]. In [24], a novel technique combining ghost penalty methods with AgFEM was proposed, offering reduced sensitivity to stabilization parameters compared to standard ghost methods.

In the body-fitted case, one can consider variational space-time formulations [25, 26, 27] to avoid the generation of 4D meshes. In these formulations, a body-fitted mesh is extruded using a geometric mapping technique to represent the temporal evolution of the boundary displacements. However, when dealing with large displacements, the geometric mapping process becomes ill-posed, often necessitating re-meshing. Similar challenges arise in body-fitted arbitrary Lagrangian Eulerian (ALE) [28, 29] schemes, where frequent re-meshing becomes necessary due to large changes in topology. Consequently, none of these formulations are robust when confronted with large displacements. Furthermore, the re-meshing process introduces bottlenecks within the simulation procedure and incurs in projection errors when transferring between meshes.

Despite the notable advantages of unfitted FEMs, its application in the space-time domain [30, 31] is currently limited to implicit level set geometrical representations (in which 4D geometrical treatment is attainable), 2D explicit representations (in which 3D geometrical tools, e.g., in [12], can readily be used for space-time) or piecewise constant approximations of the geometry in time [32]. This limitation stems from the complexity involved in developing 4D geometrical tools for unfitted methods with explicit boundary representations.

The present work introduces a novel variational space-time formulation for unfitted FEMs that eliminates the need for complex 4D geometrical algorithms. Instead, our formulation relies on time-extruded FE spaces. Furthermore, we incorporate an *exact* inter-slab transfer mechanism through an intersection algorithm, which removes projection errors between time slabs. The main contributions of our work are as follows:

- We develop space-time formulations for unfitted FEMs on moving 3D geometries described explicitly.
- We propose to pull back the problem to a reference configuration that is constant in each time slab to avoid 4D geometrical algorithms.
- We propose and implement an exact time slab transfer mechanism that relies on 3D intersection algorithms.
- We compute the solution of transient problems on complex unfitted domains with large displacements.

The outline of this paper is as follows. In Section 2, we introduce the geometry description and the space-time FE spaces employed in this work. In Section 3, we present the variational formulation through a model problem. We also define the integration measures and the inter-slab transfer mechanism. In Section 4, we describe the intersection algorithm for time slab transfer. Then, in Section 5, we present numerical results for space and time convergence, condition number tests, and a numerical example of a moving domain. Finally, in Section 6, we present our conclusions and future work.

2. SPACE TIME UNFITTED FINITE ELEMENT METHOD

In this section, we introduce the geometry description by utilizing a geometrical map defined in a space-time FE space. We also define the unfitted space-time FE spaces that are necessary to support our proposed formulation.

2.1. Geometry description for moving domains. Let us consider an initial Lipschitz domain Ω_0 in a description suitable for unfitted FEM. Following the methodology described in [12], we assume that Ω_0 is represented by a parameterized surface, e.g., a stereolithography (STL) mesh or a CAD model. For simplicity, we consider an oriented surface mesh \mathcal{B}_h^0 where the interior corresponds to the domain Ω_0 . Let $[0, T]$ be the time interval of interest.

We consider the coordinates of the mesh nodes of \mathcal{B}_h to be time-dependent. Consequently, $\mathcal{B}_h(t)$ and its corresponding interior $\Omega(t)$. This variation of coordinates can be represented by a map $\mathbf{D} : \mathcal{B}_h(0) \times [0, T] \rightarrow \mathcal{B}_h(t)$ such that $\mathbf{D}(\cdot, 0)$ is the identity.

Next, we define the space-time domain $Q = \{x \in \Omega(t) : t \in [0, T]\}$, in accordance with the nomenclature in [30], see Fig. 1. Additionally, we partition the boundary of the domain $\partial\Omega(t)$ into Dirichlet and Neumann boundaries, $\partial\Omega_D(t)$ and $\partial\Omega_N(t)$, resp. This partition is such that $\partial\Omega(t) = \partial\Omega_D(t) \cup \partial\Omega_N(t)$ and $\partial\Omega_D(t) \cap \partial\Omega_N(t) = \emptyset$. The space-time boundaries are defined as $\partial Q_* \doteq \bigcup_{t \in [0, T]} \partial\Omega_*(t) \times \{t\}$ for $*$ $\in \{N, D\}$. Consequently, the boundary of Q is given by $\partial Q \doteq \Omega(0) \cup \Omega(T) \cup \partial Q_D \cup \partial Q_N$.

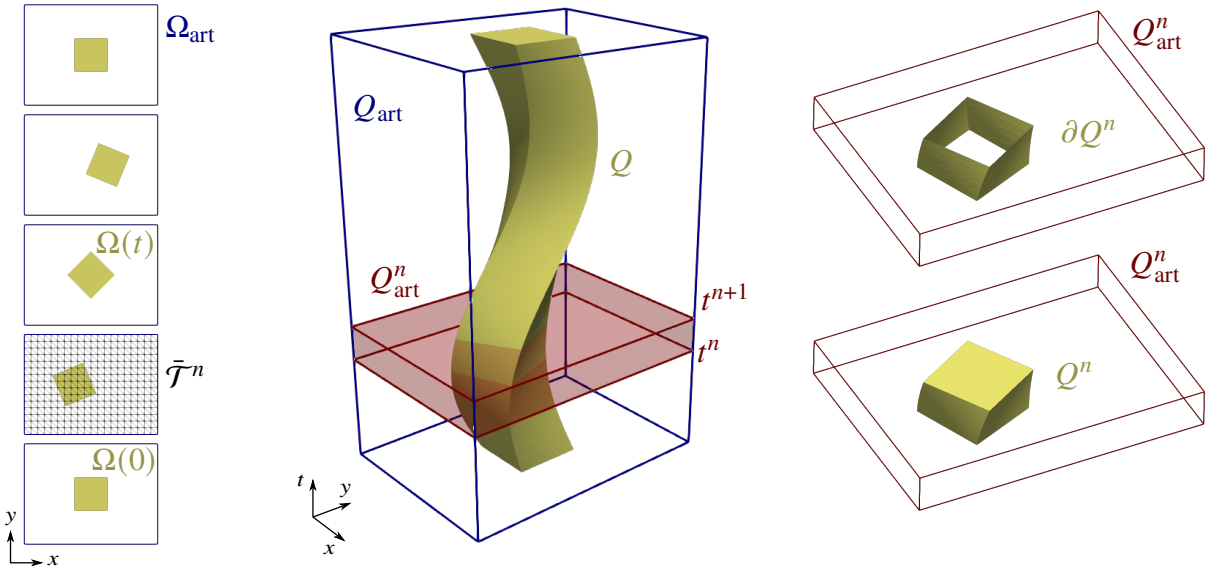


FIGURE 1. Representation of the space-time domain Q embedded within an artificial space-time domain Q_{art} . The spacial domains $\Omega(t)$ and Ω_{art} in 2D are extruded in the time dimension. The solution is computed in each time slab $J^n = (t^n, t^{n+1})$ on the space-time domain Q^n , which is embedded in Q_{art} .

In addition, we introduce an artificial spatial domain Ω_{art} , such that $\Omega(t) \subset \Omega_{\text{art}}$ for all $t \in [0, T]$. This artificial domain can be a simple geometric shape, such as a bounding box, that can conveniently be meshed with a regular grid, such as a Cartesian mesh. Subsequently, we define the artificial space-time domain $Q_{\text{art}} \doteq \Omega_{\text{art}} \times [0, T]$, such that $Q \subset Q_{\text{art}}$.

We define a partition in time, $\{J^n\}_{n=1}^N$ for $[0, T]$, in which the time domain is divided into time slabs. The time slabs are defined as $J^n = (t^n, t^{n+1})$, $1 < n < N$ where $t^n < t^{n+1}$, $\forall n \in 1, \dots, N$. Within each time slab, the time-step size is defined as $\tau^n = t^{n+1} - t^n$ and the domain time-step size is defined as $\tau = \max_{n=1, \dots, N} \tau^n$. In each time slab, we define an artificial space-time domain $Q_{\text{art}}^n \doteq \Omega_{\text{art}} \times J^n$. In a time slab, the space-time domain is determined by $Q^n \doteq Q_{\text{art}}^n \cap Q$. Similarly, the space-time boundary is denoted as $\partial Q_{\{D, N\}}^n$. We also introduce the notation $\Omega^n \doteq \Omega(t^n)$, $n = 1, \dots, N + 1$.

Finally, we define an undeformed space-time domain at each time slab as $\hat{Q}^n \doteq \Omega^n \times J^n$, see Fig. 2. Here, we note that Ω^n is the initial spatial domain of the time slab $J^n = (t^n, t^{n+1})$. In order to define the reference configuration, we require a map $\varphi_h^n : \hat{Q}^n \rightarrow Q^n$ that must satisfy

$$\varphi_h^n(\partial\Omega(t)) = D(t)(\mathcal{B}_h^0),$$

i.e., respect the boundary position determined by D .

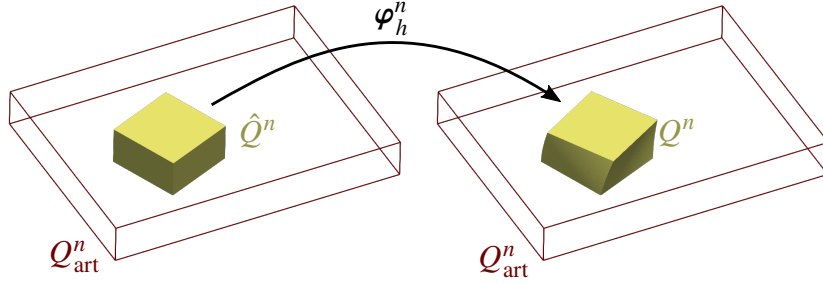


FIGURE 2. Representation of the deformation map φ_h^n resulting from extending the variation of the surface map D in the time slab domain Q^n (or in the time slab artificial domain Q_{art}^n). The undeformed configuration \hat{Q}^n will be used for the FE analysis.

Let $\bar{\mathcal{T}}_{\text{art}}^n$ represent a simple partition of Ω_{art} at time t^n . Even though Ω_{art} does not evolve in time, the partition $\bar{\mathcal{T}}_{\text{art}}^n$ can differ across time slabs, e.g., when using adaptive mesh refinement (AMR) techniques. We define the partition of Q_{art}^n as a Cartesian product of $\bar{\mathcal{T}}_{\text{art}}^n$ and J^n . Specifically, $\mathcal{T}_{\text{art}}^n \doteq \{\bar{K} \times J^n : \bar{K} \in \bar{\mathcal{T}}_{\text{art}}^n\}$. We can classify the spatial artificial cells $K \in \bar{\mathcal{T}}_{\text{art}}^n$ as interior, cut, and exterior depending on the relative position concerning the domain boundary $\partial\Omega^n$. Since there is a one-to-one map between cells in $\bar{\mathcal{T}}_{\text{art}}^n$ and $\mathcal{T}_{\text{art}}^n$, it already provides a classification of the cells in the space-time artificial mesh $\mathcal{T}_{\text{art}}^n$, which corresponds to the in-out classification for the extruded space-time domain boundary $\partial\hat{Q}^n$.

In the context of unfitted FEM, we are interested in solving partial differential equations (PDEs) using the active portion of $\mathcal{T}_{\text{art}}^n$, i.e., the cells touching Ω^n at t^n . Thus, we remove the exterior cells $\bar{\mathcal{T}}_{\text{out}}^n \doteq \{\bar{K} \in \bar{\mathcal{T}}_{\text{art}}^n : \bar{K} \cap \Omega^n = \emptyset\}$ from the artificial spatial partition $\bar{\mathcal{T}}_{\text{art}}^n$, leading to an active spatial partition $\bar{\mathcal{T}}^n \doteq \bar{\mathcal{T}}_{\text{art}}^n \setminus \bar{\mathcal{T}}_{\text{out}}^n$. From the spatial active partition, we compute the active space-time partition $\mathcal{T}^n \doteq \{\bar{K} \times J^n : \bar{K} \in \bar{\mathcal{T}}^n\}$ by extrusion.

2.2. Space-time finite element spaces. In this section, we define space-time unfitted FE spaces for the discretization of the model problem on moving domains. However, a main difference with respect to [30], the original problem on Q^n will be re-state in the undeformed domain \hat{Q}^n . As a result, in this section, we only need a construction that works on time-extruded domains. Thus,

the active mesh \mathcal{T}^n is the one that intersects Ω^n at t^n , as defined above. We note that \mathcal{T}^n may change across time slabs in evolving domains.

Firstly, we define the FE space \mathcal{X}_h^n in the spatial domain. Then, for each degree of freedom (DOF) in \mathcal{X}_h^n , we introduce a 1D FE basis \mathcal{Y}_τ^n . Thus, we construct the space-time FE space composed as the tensor product of these two spaces, $\mathcal{V}_h^n \doteq \mathcal{X}_h^n \otimes \mathcal{Y}_\tau^n$.

In each space-time cell $T^n = \bar{T}^n \times J^n \in \mathcal{T}^n$, we can define the FE local interpolation, which consists of tensor product DOFs $\Sigma \doteq \Sigma_X \otimes \Sigma_Y$ and shape functions $\Phi \doteq \Phi_X \otimes \Phi_Y$. Specifically, any shape function $\phi \in \Phi$ can be expressed as $\phi^{(\alpha_X, \alpha_Y)}(\mathbf{x}, t) = \phi_X^{\alpha_X}(\mathbf{x}) \otimes \phi_Y^{\alpha_Y}(t)$.

To address the ill-conditioning issues in unfitted FEM, we will utilize as a model example the AgFEM, even though the proposed numerical framework can readily be used for other techniques, e.g., ghost penalty stabilization (see [30] for space-time unfitted formulations). The AgFEM eliminates problematic DOFs by constraining them to well-posed DOFs using a discrete extension operator \mathcal{E} . We define the spatial extension operator $\bar{\mathcal{E}} : \bar{\mathcal{V}}_{h,\text{in}} \mapsto \bar{\mathcal{V}}_h$ between the the spatial interior $\bar{\mathcal{V}}_{h,\text{in}}$ and active $\bar{\mathcal{V}}_h$ FE spaces. The spatial aggregated finite element (AgFE) space is defined as $\bar{\mathcal{V}}_{h,\text{ag}} \doteq \bar{\mathcal{E}}(\bar{\mathcal{V}}_{h,\text{in}})$.

We define a slab-wise space-time discrete operator between $\mathcal{V}_{h,\text{in}}^n$ and \mathcal{V}_h^n . In each time slab, we aggregate the cut cells in the spatial active mesh $\bar{\mathcal{T}}^n$ using the aggregation techniques from the AgFEM. For a given time slab J^n , the space-time extension operator $\mathcal{E}^n : \mathcal{V}_{h,\text{in}}^n \mapsto \mathcal{V}_h^n$ is defined as

$$\mathcal{E}^n(\mathcal{V}_{h,\text{in}}^n) = \mathcal{E}^n(\bar{\mathcal{V}}_{h,\text{in}}^n \otimes \mathcal{Y}_\tau^n) = \bar{\mathcal{E}}^n(\bar{\mathcal{V}}_{h,\text{in}}^n) \otimes \mathcal{Y}_\tau^n,$$

where $\bar{\mathcal{E}}^n : \bar{\mathcal{V}}_{h,\text{in}}^n \mapsto \bar{\mathcal{V}}_h^n$ represents the spatial extension operator, and \mathcal{Y}_τ^n the FE space in time at the time slab J^n . We define the space-time AgFE space on the time slab. Now, we can define the global AgFE space as $\mathcal{V}_{h,\text{ag}} \doteq \mathcal{V}_{h,\text{ag}}^1 \times \cdots \times \mathcal{V}_{h,\text{ag}}^N$. Note that no continuity is imposed across time slabs, i.e., the discrete time space is discontinuous.

In ghost penalty formulations, one can readily use the non-aggregated spaces on the active mesh and add stabilization terms (see, e.g., [33]) to make the problem robust with respect to cut locations. Thus, the space-time FE spaces to be used in this case is simply \mathcal{V}_h^n .

2.3. Extension of the deformation map. In the case in which the domain is represented in time by its explicit boundary representation and its boundary displacement $\mathbf{D}(t)$, we must extend $\mathbf{D}(t)$ defined on $\mathcal{B}(t)$ to the space-time domain \hat{Q}^n of each time slab J^n . For this purpose, we solve the following linear elasticity problem in \hat{Q}^n , even though other extension operators could be considered. Find $\hat{\mathbf{u}} \in \mathbb{R}^d$ such that,

$$\begin{cases} \hat{\nabla}_x \cdot \boldsymbol{\sigma}(\hat{\mathbf{u}}) = 0 & \text{in } \hat{Q}^n, \\ \hat{\mathbf{u}} = \hat{\mathbf{u}}_D^n & \text{on } \partial \hat{Q}_D^n, \\ \hat{\mathbf{u}} = 0 & \text{on } \partial \hat{Q}_{D_0}^n, \\ \mathbf{n}_x \cdot \boldsymbol{\sigma}(\hat{\mathbf{u}}) = 0 & \text{on } \partial \hat{Q}_N^n. \end{cases}$$

where $\boldsymbol{\sigma}$ is the stress tensor, $\hat{\nabla}_x$ is the spatial gradient, \mathbf{n}_x is the spatial component of outward normal vector to $\partial \hat{Q}^n$, and

$$\hat{\mathbf{u}}_D^n(t) = (\mathbf{D}(t) - \mathbf{D}(t^n)) \circ (\mathbf{D}(t^n))^{-1}$$

is the Dirichlet boundary condition on $\partial \hat{Q}_D^n = \mathcal{B}_h(t^n) \times J^n$, which imposes the deformation near the unfitted boundary (see Fig. 3). On the boundary of the artificial domain and at the initial spatial domain, $\partial \hat{Q}_{D_0}^n = \partial \Omega_{\text{art}} \times J^n \cup \Omega^n \times \{t^n\}$, the deformation is fixed to zero. The Neumann boundary is defined on $\partial \hat{Q}_N^n = \Omega^n \times \{t^{n+1}\}$.

This problem is approximated with a continuous Galerkin (CG) method and weak imposition of the Dirichlet boundary conditions on the unfitted boundary $\partial \hat{Q}_D$ using Nitsche's method [34].

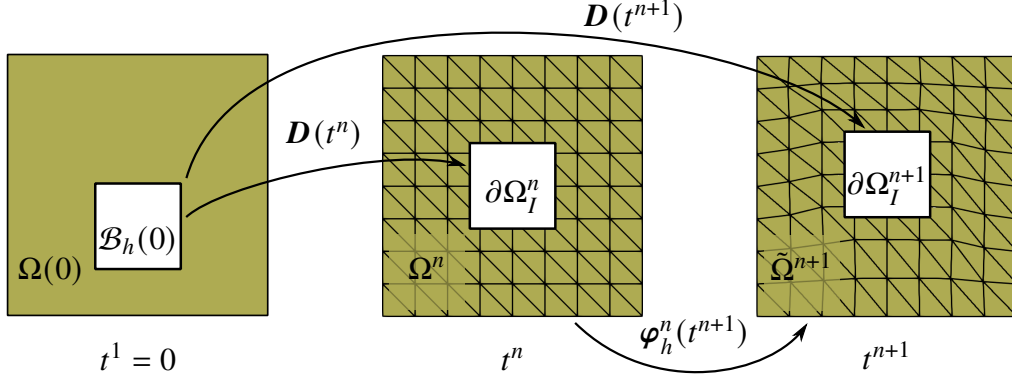


FIGURE 3. Representation of the deformation map \mathbf{D} and the extended map $\boldsymbol{\varphi}_h^n$ in the time slab $J^n = (t^{n-1}, t^n)$. This example represents the external domain. The spatial deformation map $\mathbf{D}(t) : \mathcal{B}_h(0) \mapsto \mathcal{B}_h(t)$, $t \in [0, T]$, is defined on the surface mesh, and the extended map $\boldsymbol{\varphi}_h^n(t) : \Omega^n \mapsto \tilde{\Omega}(t)$, $t \in J^n$, is defined on the spatial domain. At t^{n+1} , the description of the inner boundary $\partial\Omega_I^{n+1}$ may differ across maps: $\boldsymbol{\varphi}_h^n(t^{n+1})(\partial\Omega_I^n) \approx \mathbf{D}(t^{n+1})(\mathcal{B}_h(0))$, where $\partial\Omega_I^n = \mathbf{D}(t^n)(\mathcal{B}_h(0))$. The approximation error decreases with the spatial discretization size h .

In the weak formulation, we find $u \in \mathcal{V}_{h,\text{ag}}^n$ such that,

$$a(\hat{\mathbf{u}}, \hat{\mathbf{v}}) = l(\hat{\mathbf{v}}), \quad \forall \hat{\mathbf{v}} \in \mathcal{V}_{h,\text{ag}}^n$$

where the bilinear form and the linear form are defined as,

$$a(\hat{\mathbf{u}}, \hat{\mathbf{v}}) = \int_{\hat{Q}^n} \boldsymbol{\varepsilon}(\hat{\mathbf{v}}) : \boldsymbol{\sigma}(\boldsymbol{\varepsilon}(\hat{\mathbf{u}})) d\hat{\mathbf{x}} dt + \int_{\partial\hat{Q}_D} (\tau_D \hat{\mathbf{v}} \cdot \hat{\mathbf{u}} - \nu \cdot (\mathbf{n}_x \cdot \boldsymbol{\sigma}(\boldsymbol{\varepsilon}(\hat{\mathbf{u}})))) d\hat{\mathbf{x}} dt,$$

and

$$l(\hat{\mathbf{v}}) = \int_{\partial\hat{Q}_D} (\hat{\mathbf{v}} \cdot \hat{\mathbf{u}}_D - \mathbf{n}_x \cdot \boldsymbol{\sigma}(\boldsymbol{\varepsilon}(\hat{\mathbf{v}})) \cdot \hat{\mathbf{u}}_D) d\hat{\mathbf{x}} dt,$$

resp., where $\boldsymbol{\varepsilon}$ is the symmetric (spatial) gradient operator.

From the approximated solution $\hat{\mathbf{u}}_h^n \in \mathcal{V}_{h,\text{ag}}^n$ we extract the map $\boldsymbol{\varphi}_h^n(\hat{\mathbf{x}}, t) = \hat{\mathbf{x}} + \hat{\mathbf{u}}_h^n(\hat{\mathbf{x}}, t)$. One can alternatively use a ghost penalty stabilization to solve the elasticity problem. Since the deformation is imposed weakly, the deformation $\hat{\mathbf{u}}_h^n$ is not equal to $\hat{\mathbf{u}}_D^n$ on $\mathcal{B}_h(t)$. Thus, the deformed space-time domain Q^n is approximated by $\tilde{Q}^n = \boldsymbol{\varphi}_h^n(Q^n)$. In any case, the geometrical error is expected to decrease with the mesh size h . For given time $t \in J^n$, we can extract the spatial map $\boldsymbol{\varphi}_h^n(t) : \Omega^n \mapsto \tilde{\Omega}(t)$ (see Fig. 3). Here, the spatial domain is also approximated, $\Omega(t) \approx \tilde{\Omega}(t)$.

We assume that the computed map is one-to-one, i.e., $\det(\nabla \boldsymbol{\varphi}_h^n) > 0$ at all times. Assuming that \mathbf{D} is such that it admits an extension that is diffeomorphic, this requirement can be attained for small enough time steps in the time-discrete problem. One can also move back to the Cartesian mesh after several time steps, as soon as the map remains bijective.

2.4. Extended active mesh. As discussed above, in the case in which the deformation map has to be computed, $\boldsymbol{\varphi}_h^n$ is not equal to \mathbf{D} on $\mathcal{B}_h(t)$, since unfitted methods usually make use of weak imposition of boundary conditions.

At the end of the time slab J^n , we can define the solution in the approximated domain \tilde{Q}^n as

$$u_h^{n+1,-}(\mathbf{x}) = \hat{u}_h^n(\boldsymbol{\varphi}_h^n(t^{n+1})^{-1}(\mathbf{x}), t^{n+1}), \quad \forall \mathbf{x} \in \tilde{\Omega}^{n+1},$$

which is a function defined on the undeformed domain Ω^n ; since we integrate the forms on \hat{Q}^n , the inverse map is never computed in practice. On the other side, with the method proposed below, we have to compute an inter-slab integral on Ω^{n+1} that involves $u_h^{n+1,-}$.

In order for $u_h^{n+1,-}$ to be defined on Ω^{n+1} , we proceed as follows. First, we extend the active mesh by $\tilde{\mathcal{T}}_{\text{ext}}^n = \tilde{\mathcal{T}}^n \cup \{K \in \tilde{\mathcal{T}}_{\text{art}}^n : \varphi^n(t^{n+1})(K) \cap \Omega^{n+1} \neq \emptyset\}$. Assuming that the geometrical map is one-to-one, the inverse $\varphi_h^n(t^{n+1})^{-1}$ is well-defined on Ω^{n+1} .

To accommodate a FE space $\mathcal{V}_{h,\text{ext}}^n$ in $\tilde{\mathcal{T}}_{\text{ext}}^n$, one can consider the modification of the extension operator. In the AgFEM framework, we can simply redefine the extension operator $\bar{\mathcal{E}}_{\text{ext}}^n : \mathcal{V}_{h,\text{in}}^n \mapsto \mathcal{V}_{h,\text{ext}}^n$. In non-aggregated methods like CutFEM, we can utilize the same extension on the solution $\bar{\mathcal{E}}_{\text{ext}}^n(\mathcal{V}_h^n)$.

We note that the implementation of the extended triangulation and FE space can be computed a posteriori, on demand, whenever it is needed. One can mark the additional cells that are needed for the extension, and then extend the aggregates to these cells.

3. VARIATIONAL FORMULATION ON A MODEL PROBLEM

In this section, we establish the space-time variational formulation by employing a model problem, specifically the heat equation. Although we use the heat equation for demonstration purposes, it is essential to note that a similar approach can be applied to other PDEs.

3.1. Weak formulation. In order to define the space-time variational formulation, we first define the convection-diffusion equation in a space-time domain Q , as find u such that,

$$\begin{cases} \partial_t u + (\mathbf{w} \cdot \nabla_x)u - \mu \Delta_x u = f & \text{in } Q, \\ u = u_D & \text{on } \partial Q_D, \\ \mu \mathbf{n}_x \cdot \nabla_x u = g_N & \text{on } \partial Q_N, \\ u = u_0 & \text{on } Q(0). \end{cases} \quad (1)$$

where μ is the diffusion coefficient, \mathbf{w} the advection velocity, f the source term, u_D the Dirichlet boundary condition, and g_N boundary flux on ∂Q_N . ∇_x and Δ_x denote the spatial gradient and spatial Laplacian, resp. Well-posedness requires that $\mathbf{w} \cdot \mathbf{n}_x + n_t \geq 0$ on the Neumann boundary ∂Q_N . Here, $\mathbf{n} = (\mathbf{n}_x, n_t)$ is the outward normal to ∂Q .

We discretize this problem with the AgFEM in space (or a ghost penalty stabilization) and a DG method in time. We weakly impose the Dirichlet boundary conditions using Nistche's method [34]. Since the coupling between time slabs respects causality, we analyze the problem on a single time slab, assuming we know the solution of the previous one (see also [30]). To analyze each time slab $J^n = (t^n, t^{n+1})$, we define the problem in the reference domain $\hat{Q}^n = (\varphi_h^n)^{-1}(\tilde{Q}^n)$ as: find $\hat{u} \in \mathcal{V}_{h,\text{ag}}^n$ such that

$$B_h^n(\hat{u}, \hat{v}) = L_h^n(\hat{v}), \quad \forall \hat{v} \in \mathcal{V}_{h,\text{ag}}^n,$$

with $u = \hat{u} \circ (\varphi_h^n)^{-1}$. The bilinear form reads as:

$$\begin{aligned} B_h^n(\hat{u}, \hat{v}) &= \int_{\hat{Q}^n} \hat{v} \partial_t^n \hat{u} |J_{\hat{Q}^n}| d\hat{\mathbf{x}} dt + \int_{\Omega^n} \hat{v}(t^n) \hat{u}(t^n) |J_{\Omega^n}| d\hat{\mathbf{x}} + a_h(\hat{u}, \hat{v}), \\ a_h(\hat{u}, \hat{v}) &= \int_{\hat{Q}^n} (\mu \nabla_x^n \hat{u} \cdot \nabla_x^n \hat{v} + \hat{v}(\mathbf{w} \circ \varphi_h^n \cdot \nabla_x^n) \hat{u}) |J_{\hat{Q}^n}| d\hat{\mathbf{x}} dt \\ &\quad + \int_{\partial \hat{Q}_D^n} (\beta_h \hat{v} \hat{u} - \hat{v}(\mathbf{n}_x^n \cdot \mu \nabla_x^n \hat{u}) - (\mathbf{n}_x^n \cdot \mu \nabla_x^n \hat{v}) \hat{u}) |J_{\partial \hat{Q}_D^n}| d\hat{\mathbf{x}} dt, \end{aligned} \quad (2)$$

and the linear form reads as,

$$\begin{aligned} L_h^n(\hat{v}) &= \int_{\Omega^n} \hat{v}(t^n) \hat{u}^{n-1}(t^n) |J_{\Omega^n}| d\hat{\mathbf{x}} + l_h(\hat{v}), \\ l_h(\hat{v}) &= \int_{\tilde{Q}^n} \hat{v} (f \circ \boldsymbol{\varphi}_h^n) |J_{\tilde{Q}^n}| d\hat{\mathbf{x}} dt + \int_{\partial \tilde{Q}_N^n} \hat{v} (g_N \circ \boldsymbol{\varphi}_h^n) |J_{\partial \tilde{Q}_N^n}| d\hat{\mathbf{x}} dt \\ &\quad + \int_{\partial \tilde{Q}_D^n} (\beta_h \hat{v} (u_D \circ \boldsymbol{\varphi}_h^n) - (\mathbf{n}_x^n \cdot \mu \nabla_x^n \hat{v}) (u_D \circ \boldsymbol{\varphi}_h^n)) |J_{\partial \tilde{Q}_D^n}| d\hat{\mathbf{x}} dt, \end{aligned} \quad (3)$$

Let us define the norms used in [30] to prove stability and convergence results, which we will computed in the numerical experiments. In [30] the space-time accumulated DG norm of $\mathcal{V}_{h,\text{ag}}$ is defined as follows,

$$\|v\|_{n,*}^2 \doteq \|v^n(t^{n+1})\|_{L^2(\Omega^n)}^2 + \sum_{i=1}^n \|v^i(t^i) - v^{i-1}(t^i)\|_{L^2(\Omega^i)}^2 + c_\mu \int_0^{t^{n+1}} \|v\|_{\mathcal{V}^n(h)}^2 dt,$$

where c_μ is the coercivity constant and $\bar{\mathcal{V}}^n(h) \doteq \bar{\mathcal{V}}_{h,\text{ag}}^n + H^2(\Omega(t))$ is the norm of the FE space at a time step t given by

$$\|v\|_{\mathcal{V}^n(h)}^2 \doteq \mu \|\nabla v\|_{L^2(\Omega(t))}^2 + \sum_{\bar{T} \in \tilde{\mathcal{T}}_{h,\text{act}}^n} \beta_{\bar{T}} \|v\|_{L^2(\bar{T} \cap \partial \Omega_D(t))}^2 + \sum_{\bar{T} \in \tilde{\mathcal{T}}_{h,\text{act}}^n} \mu h_{\bar{T}}^2 \|v\|_{H^2(\bar{T} \cap \Omega(t))}^2.$$

The proof of this stability result follows the ideas in [30] in the case in which the deformation map $\boldsymbol{\varphi}_h^n(t)$ is equal to $\mathbf{D}(t)$ on $\Gamma(t)$. Otherwise, the analysis is more technical and would require to use ideas similar to the ones in [32, 35]. The analysis therein assumes a constant deformation map and a level-set description of the domain. In our case, the deformation map can be of higher-order (time-dependent) and the domain is represented by its boundary. We will leave this analysis for future work.

In the variational form, the Dirichlet boundary conditions are imposed weakly with the Nistche method, with a penalty term β_h that depends on the spatial cell size h . The initial value is also imposed weakly with DG in time, where the jump is given by $[\hat{u}(t^n) - \hat{u}^{n-1}(t^n)]$. The evaluation of the solution of the previous time slab $\hat{u}^{n-1}(t^n)$ in Ω^n requires special attention since it is computed using a different discretization. Further discussion is provided in Sect. 3.2 and Sect. 4.

The derivatives are projections of the space-time gradient into space and time, $\partial_t^n = (\nabla^n)_t$, and $\nabla_x^n = (\nabla^n)_x$, resp. They are obtained by transporting the space-time gradient to the deformed domain $\nabla^n = \mathbf{F}^{-T} \hat{\nabla}$, where $\mathbf{F} = \nabla \boldsymbol{\varphi}_h^n$. The operators $(\cdot)_x$ and $(\cdot)_t$ represent the projection to the space and time directions, resp. The boundary normal is also transported to the deformed domain. It is computed as follows,

$$\mathbf{n}_x^n = \left(\frac{\mathbf{F}^{-T} \mathbf{n}_{\partial \tilde{Q}^n}}{\|\mathbf{F}^{-T} \mathbf{n}_{\partial \tilde{Q}^n}\|} \right)_x,$$

where $\mathbf{n}_{\partial \tilde{Q}^n}$ is the normal vector in the undeformed space-time domain.

The integration measures to define the domain change are defined by the jacobians of the deformed domain. The integration measure change of the space-time domain \tilde{Q}^n is given by $J_{Q^n} = J$, where $J = \det(\mathbf{F})$. The initial boundary Jacobian is defined as $J_{\Omega^n} = \det(\mathbf{F}_x(t^n))$. In the given case $J_{\Omega^n} = 1$. Note that for small deformations, where $\min_{\Omega}(J) \approx 1$, a simpler approach can be considered by assuming a deformed initial state, e.g., $\Omega^n = \boldsymbol{\varphi}_h^{n-1}(t^n)(\Omega^{n-1})$. In this situation, the evaluation $\hat{u}_h^{n-1}(t^n)$ does not require the change of reference space described in Sect. 3.2. This approach is equivalent to a time slab with more than one cell in time and continuous FE spaces in time could be considered within this macro-cell.

The pullback of the area differential form to the reference domain is expressed as

$$da_{\partial\tilde{Q}^n} = J \sqrt{\mathbf{n}_{\partial\tilde{Q}^n}^T \cdot \mathbf{C}^{-1} \cdot \mathbf{n}_{\partial\tilde{Q}^n}} da_{\partial\hat{Q}^n}$$

where $\mathbf{C} = \mathbf{F}^T \mathbf{F}$ (see, e.g., [36]).

The space-time gradients are transported to the deformed domain, $\nabla^n = \mathbf{F}^{-T} \hat{\nabla}$. The map gradient, $\mathbf{F} = \nabla \boldsymbol{\varphi}_h^n$, contains the terms as follows:

$$\mathbf{F} = \begin{bmatrix} \mathbf{F}_x & 0 \\ \partial_t \boldsymbol{\varphi}_{h,x}^n & 1 \end{bmatrix} = \begin{bmatrix} \mathbf{F}_x & 0 \\ \mathbf{w}^T & 1 \end{bmatrix},$$

where \mathbf{F}_x is the space gradient and $\mathbf{w}^T = \partial_t \boldsymbol{\varphi}_{h,x}^n$ the deformation velocity. Then, the inverse gradient is given by

$$\mathbf{F}^{-T} = \begin{bmatrix} \mathbf{F}_x^{-1} & 0 \\ -\mathbf{w}^T \mathbf{F}_x^{-1} & 1 \end{bmatrix}.$$

Then, by decomposing the space-time gradient into space and time derivatives, we obtain

$$\begin{bmatrix} \nabla_x^n \\ \partial_t^n \end{bmatrix} = \mathbf{F}^{-T} \begin{bmatrix} \hat{\nabla}_x \\ \hat{\partial}_t \end{bmatrix} = \begin{bmatrix} \mathbf{F}_x^{-1} \hat{\nabla}_x \\ \hat{\partial}_t - \mathbf{w}^T \mathbf{F}_x^{-1} \hat{\nabla}_x \end{bmatrix},$$

which already recovers the derivative terms used in ALE formulations.

3.2. Inter-slab integration. In the formulation (2)-(3), a DG method is used in time, where the initial value at the time slab is imposed weakly through an inter-time slab jump $[\hat{u}^n(t^n) - \hat{u}^{n-1}(t^n)]$. However, integrating this jump is not straightforward, since $\hat{u}^n(t^n)$ and $\hat{u}^{n-1}(t^n)$ in (3) are expressed in different discrete spaces (and meshes).

To address this evaluation, let us introduce a time slab transfer mechanism that relies on an intermediate unfitted discretization $\tilde{\mathcal{T}}_{\text{int}}^n$. $\tilde{\mathcal{T}}_{\text{int}}^n$ is a partition of Ω^n that results of intersecting the embedded discretization $\mathcal{T}_{\text{cut}}^n$ of Ω^n and $\tilde{\mathcal{T}}_-^n = \boldsymbol{\varphi}_h^{n-1}(t^n)(\tilde{\mathcal{T}}^{n-1})$, i.e., $\tilde{\mathcal{T}}_{\text{int}}^n$ results from intersecting $\tilde{\mathcal{T}}^n$, $\tilde{\mathcal{T}}_-^n$ and Ω^{n-1} . Each cell $K_{\text{int}} \in \tilde{\mathcal{T}}_{\text{int}}^n$ has an injective map to $K^{n-1} \in \tilde{\mathcal{T}}^{n-1}$ and $K^n \in \tilde{\mathcal{T}}^n$. A representation of $\tilde{\mathcal{T}}_{\text{int}}^n$ is depicted in Fig. 4, and its construction is detailed in Sect. 4.

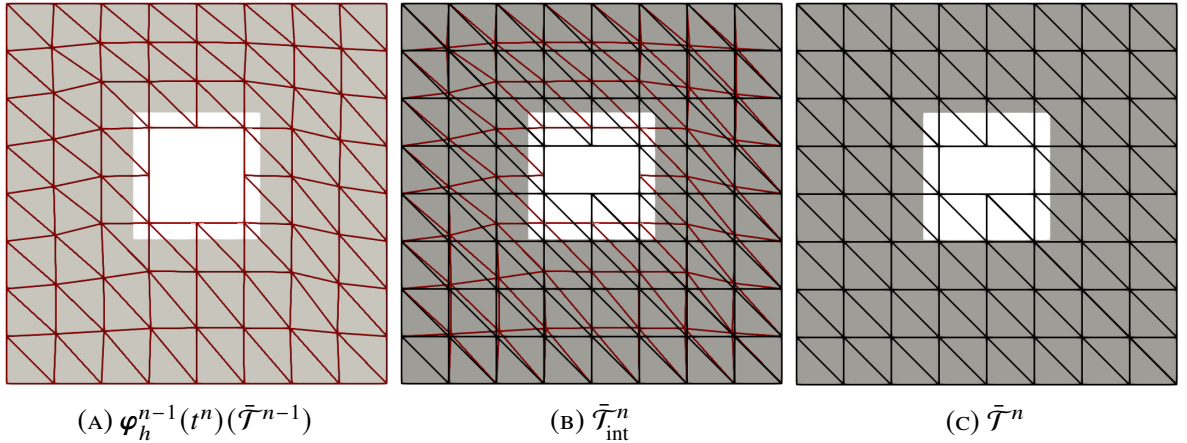


FIGURE 4. Mesh sequence for solution transfer between time slabs. The solution obtained in $\tilde{\mathcal{T}}^{n-1}$ in (a) is then evaluated at $\tilde{\mathcal{T}}^n$ (c). Acting as a bridge, the intersected mesh $\tilde{\mathcal{T}}_{\text{int}}^n = \boldsymbol{\varphi}_h^{n-1}(t^n)(\tilde{\mathcal{T}}^{n-1}) \cap \tilde{\mathcal{T}}^n \cap \Omega^n$ in (b) facilitates the evaluation by providing injective cell maps to both active meshes.

The integration of the jump in the time slab interface is performed in $\tilde{\mathcal{T}}_{\text{int}}^n$. Thus, we need to define the cell maps from $\tilde{\mathcal{T}}_{\text{int}}^n$ to $\tilde{\mathcal{T}}^n$ and $\tilde{\mathcal{T}}^{n+1}$. For $\hat{u}^{n-1}(t^n)$ we need a cell map from $\hat{K}_{\text{int}} \in \tilde{\mathcal{T}}_{\text{int}}^n$

Algorithm 2 in [12]. Alternatively, in line 10, we intersect the cells $K \in \mathcal{T}$ within the domain $\text{int}(\mathcal{B})$ bounded by \mathcal{B} that are not intersected by the domain boundary \mathcal{B} . The information about the cells inside $\text{int}(\mathcal{B})$ is obtained from the propagation through the untouched cells (see [12]). The returned triangulation \mathcal{T}_{int} not only covers the cells cut cells intersected by the boundary \mathcal{B} but the entire domain enclosed by \mathcal{B} . This process guarantees that each cell $K_{\text{int}} \in \mathcal{T}_{\text{int}}$ has an injective map to $K \in \mathcal{T}$ and $K_- \in \mathcal{T}_-$. The cells in \mathcal{T}_{int} are general polytopes that cannot use standard quadrature rules. In order to numerically integrate in these cells, one can perform a decomposition of the cells into simplices. Alternatively, one can reduce the dimension of the integrals with Stokes theorem and moment-fitting methods; see more details in [13] and references therein.

Algorithm 1 $\mathcal{T} \cap \mathcal{T}_- \cap \text{int}(\mathcal{B})$

```

1:  $\mathcal{T}_{\text{cut}} \leftarrow \emptyset, \quad \mathcal{T}_{\text{in}} \leftarrow \emptyset$ 
2: for  $K \in \mathcal{T}$  do
3:    $\mathcal{B}^K \leftarrow \text{restrict}(\mathcal{B}, K)$ 
4:    $\mathcal{T}_-^K \leftarrow \text{restrict}(\mathcal{T}_-, K)$ 
5:    $\mathcal{T}_{\text{cut}}^K \leftarrow K \cap \text{int}(\mathcal{B}^K)$ 
6:   for  $K_- \in \mathcal{T}_-^K$  do
7:     if  $K \cap \mathcal{B} \neq \emptyset$  then
8:        $\mathcal{T}_{\text{cut}}^{K, K_-} \leftarrow \{K_{\text{cut}} \cap K_- : K_{\text{cut}} \in \mathcal{T}_{\text{cut}}^K\}; \quad \mathcal{T}_{\text{cut}} \leftarrow \mathcal{T}_{\text{cut}} \cup \mathcal{T}_{\text{cut}}^{K, K_-}$ 
9:     else if  $K \subset \text{int}(\mathcal{B})$  then
10:       $\mathcal{T}_{\text{in}} \leftarrow \mathcal{T}_{\text{in}} \cup (K \cap K_-)$ 
11:     end if
12:   end for
13: end for
14: return  $\mathcal{T}_{\text{int}} \leftarrow \mathcal{T}_{\text{cut}} \cap \mathcal{T}_{\text{in}}$ 

```

We emphasize that the intersection algorithm is as robust as the core cut algorithm in line 5. Furthermore, it is important to note that, for evaluation purposes, accurate tolerance management is not required in the intersection process of line 8. While the algorithm is described for the core cut algorithm with an exact embedded discretization of explicit domain representation [30], Alg. 1 is general enough to be used with other unfitted discretizations.

5. NUMERICAL EXPERIMENTS

5.1. Objectives. In the experiments of this section, we aim to demonstrate the effectiveness of the presented methods. In particular, we examine the following aspects within our formulation:

- We evaluate the *hp*-convergence on both 2D and 3D spatial domains, compared to the results and analysis in [30].
- We explore numerical stability concerning the cut location and the approximation degrees.
- We assess the applicability of our formulation to complex 2D and 3D moving domains derived from STL models.

It is important to note that these experiments focus on comparing our formulation with the one presented in [30]. Recall that [30] uses space-time embedded discretizations on implicit geometries determined by level sets, and the results are presented exclusively in 2D+1D domains (as the geometrical algorithms for 3D+1D domains are significantly more complex). In contrast, we design a space-time formulation that works on explicit boundary representations and only require geometrical intersection algorithms in space only, e.g., 2D and 3D vs. 3D and 4D in [30]. This is possible by pulling back the problem into an extruded space-time domain using the formulation in Sect. 3.1.

5.2. Environment setup. The numerical experiments have been performed on Gadi and Titani supercomputers. Gadi is a high-end supercomputer at the NCI (Australia) with 4962 nodes, 3074 of them powered by a 2 x 24 core Intel Xeon Platinum 8274 (Cascade Lake) at 3.2 GHz and 192 GB RAM. Titani is located at UPC (Spain) with 6 nodes, 5 of them powered by a 2 x 12 core Intel Xenon E5-2650L v3 at 1.8 GHz and 256 GB RAM. The algorithms presented in this work have been implemented in the Julia programming language [38]. The unfitted FE computations have been performed using the Julia FE library `Gridap.jl` [39] version 0.17.17 and the extension package for unfitted methods `GridapEmbedded.jl` version 0.8.1 [40]. `STLCutters.jl` version 0.1.6 [41] has been used to compute intersection computations on STL geometries. To mitigate excessive computational costs, the condition numbers are computed in the 1-norm using `cond()` Julia function.

5.3. Space-time convergence tests. To demonstrate optimal convergence rates we solve a simple PDE with a manufactured solution out of the FE space. Inspired by [30], we solve the Poisson equation (1) with the following manufactured solution

$$u(x, t) = \sin\left(\frac{\pi\alpha t}{T}\right) \prod_{i=1}^D \sin\left(\frac{\pi x_i}{L_i}\right),$$

where $\{L_1, \dots, L_D, T\}$ are the cartesian dimensions of the space-time domain and the time parameter is set to $\alpha = 0.5$ for the experiments shown in Fig. 6 and Fig. 7. Furthermore, in the equation (1) we set the diffusion term as $\mu = 1$. The space domain is a n -cube with a n -cubic hole in the center. The hole is described by the STL of a cube. The lengths at the domain sides are $L = 3$ while the lengths of the hole sides are $l = 1$. The time domain has size $T = 1$. The hole is linearly translated in the x direction. The displacement map is described as $\mathbf{D}(x, t) = (0.2t, 0, 0)$. In all the cases, the domain discretization is a regular Cartesian grid, with the same number of elements n in each direction, both space and time.

For implementation reasons, the two-dimensional examples are computed with a three-dimensional STL. Thus, we build a pseudo-two-dimensional domain that has only one cell in the z direction. The space-time domain dimensions are $\{L, L, \frac{L}{n}, T\}$ while the number of elements in each direction is $\{n, n, 1, n\}$. The number of elements per direction in convergence tests is $n = 2^i, i = 3, \dots, 6$ in two-dimensional runs, while $n = 2^i, i = 3, \dots, 5$ for three-dimensional runs.

We analyze the condition number of the system to be inverted in each time slab. Since the system matrix is nonsymmetric, as suggested in [30], a preconditioner for DG in time [42] can be considered. The effectiveness of this preconditioner depends on the condition numbers the mass and stiffness matrices, which are defined as follows,

$$\mathbf{M}_{ab} = \int_{\hat{Q}^n} \mathcal{E}^n(\Phi^a) \mathcal{E}^n(\Phi^b) |J_{\Omega^n}| d\hat{\mathbf{x}} dt, \quad \mathbf{A}_{ab} = a_h \left(\mathcal{E}^n(\Phi^a), \mathcal{E}^n(\Phi^b) \right).$$

The condition numbers presented in Fig. 6a and Fig. 6b are computed in the initial time slab of the two-dimensional convergence experiments. We observe that the condition number of the mass matrix remains nearly constant, while the condition number of the stiffness matrix scales with $\mathcal{O}(h^{-2})$. These observations align with the behavior expected for AgFEM in space-time domains analyzed in [30].

Now, let us analyze the convergence of the error norms. In Fig. 6, we can observe the accumulated DG error norm convergence with coercivity constant $c_\mu = 1$. We observe that using the AgFEM and constant h/τ the error converges with $\mathcal{O}(h^r)$, where the convergence rate $r = \min(p, q)$. Fig. 7 shows the $L^2(\Omega^n)$ and $H^1(\Omega^n)$ norms at the final time $t = T$. The convergence rate of $L^2(\Omega^n)$ norm is $r = \min(p, q) + 1$ while the convergence rate of $H^1(\Omega^n)$ norm is $r = p$. These results are in agreement with the theoretical and analytical space-time AgFEM results in [23].

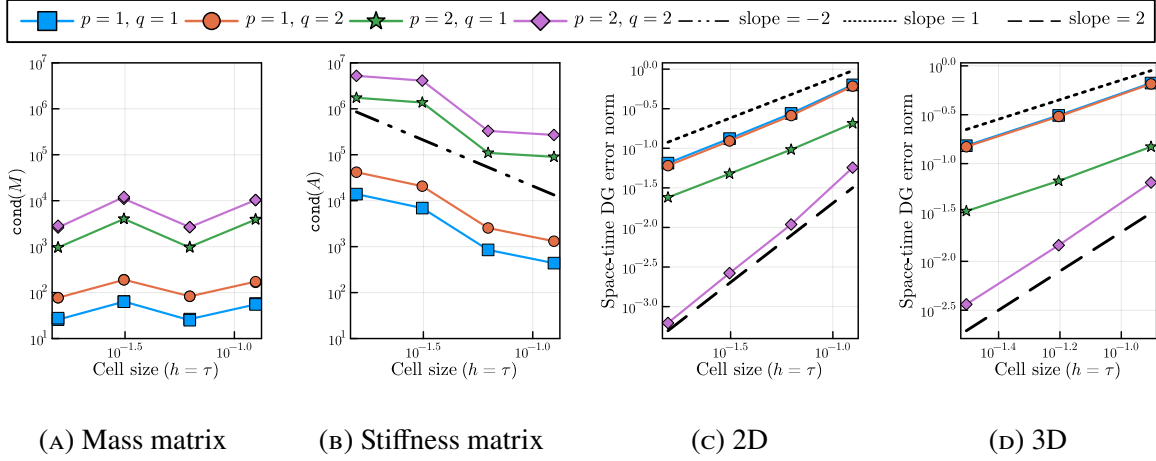


FIGURE 6. Scaling of the condition numbers of the mass and stiffness matrices in the initial time slab, (a) and (b). Convergence of the space-time DG norm error ($e = u - u_h$) in two and three-dimensional space domains (c) and (d). Here, p and q represent the space and time approximation order, resp.

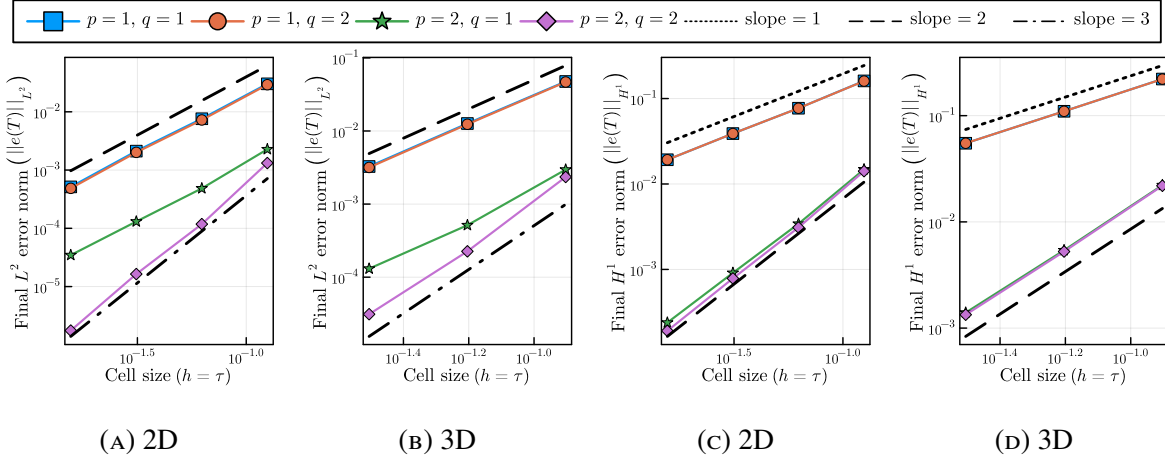


FIGURE 7. Convergence of the $L^2(\Omega^n)$ and $H^1(\Omega^n)$ norms of the error ($e = u - u_h$) at the final time $t = T$ in two and three-dimensional space domains. Here, p and q represent the space and time approximation order, resp.

5.4. Moving domains examples. To demonstrate the applicability of the presented algorithms for the simulation of fluids around moving boundaries, we solve the flow around two rotating geometries in 2D and 3D. We solve the Navier-Stokes and Stokes equations resp. with kinematic viscosity $\nu = 10^{-2}$. Regardless of the dimension, we run similar setups. Both share the same discretization order for pressure $p_p = 1$, velocity $p_u = 2$ and time q . We utilize the AgFEM aggregating all cut cells.

We improve the accuracy of both meshes by clustering the cells around the geometry. See Fig. 8 and Fig. 9 for 2D and 3D, resp. We map each direction $i \in 1, \dots, d$ of the Cartesian meshes as follows,

$$\phi_M^i(\hat{x}) = \begin{cases} \hat{x}_0^i \left(\frac{\hat{x}^i}{\hat{x}_0^i} \right)^\alpha & \text{if } \hat{x}^i < \hat{x}_0^i, \\ 1 - (1 - \hat{x}_0^i) \left(\frac{1 - \hat{x}^i}{1 - \hat{x}_0^i} \right)^\alpha & \text{otherwise.} \end{cases} \quad (4)$$

Here, $\hat{x}^i = x^i - x_0^i/L^i$ is the reference axis of the direction x^i where x_0^i is the lower value in the i direction, and L^i is the i -length. In (4), we use $\hat{x}_0^i = 0.5$ to determine the region of element condensation and the exponential factor $\alpha < 1$ for the smoothness of the map.

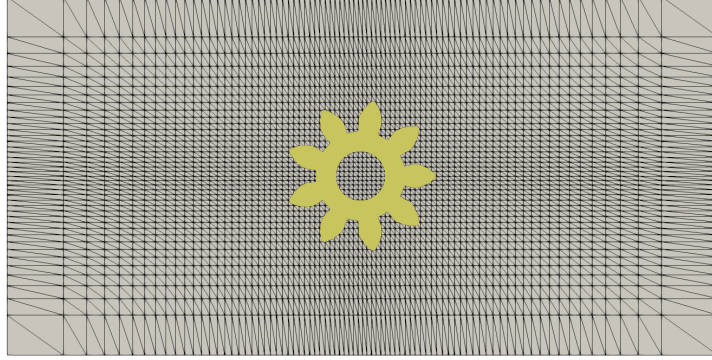


FIGURE 8. Background spatial mesh $\bar{\mathcal{T}}^{\text{bg}}$ around a prismatic gear \mathcal{B}_0 (geometry id 71711 from *Thingi10k* [43]). This mesh is the simplex partition of a mapped Cartesian mesh. The uniform elements are mapped in each direction with ϕ_M (4) and an exponential factor $\alpha = 0.5$. The Cartesian mesh has 80×40 elements before the simplex decomposition. The artificial domain Ω^{art} is a box of size $4.8L_x \times 2.4L_y$. Here, L_x and L_y represent the bounding box size of \mathcal{B}_0 .

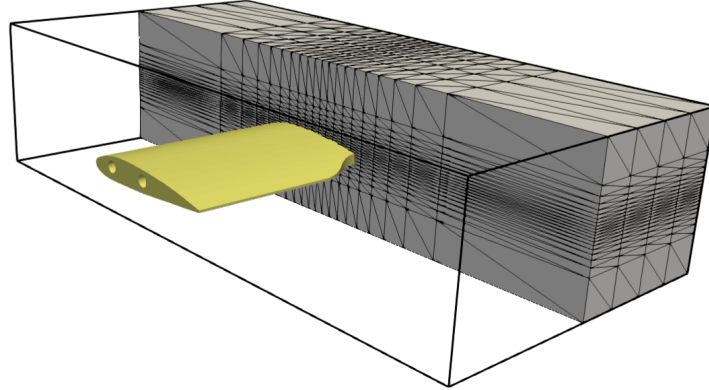


FIGURE 9. Background spatial mesh $\bar{\mathcal{T}}^{\text{bg}}$ around a wing \mathcal{B}_0 (id 65604 in *Thingi10k*). This simplex mesh comes from a mapped Cartesian mesh. The coordinates of the mesh are mapped in the x and y directions with ϕ_M (4) and an exponential factor $\alpha = 0.3$. The Cartesian mesh has $20 \times 20 \times 8$ elements. The artificial domain Ω^{art} is a box of size $4L_x \times 4L_y \times 0.8L_z$. Here, L_x , L_z and L_y represent the bounding box size of \mathcal{B}_0 .

In the 2D example of Fig. 8 and Fig. 10, we solve the Navier-Stokes equations with $Re = 10^2$. We define a parabolic inlet flow in the x -direction,

$$u(\mathbf{x}) = U_{\max}(4x_2 - 4x_2^2),$$

where $U_{\max} = (1, 0, 0)$. We set zero velocity on the y -faces and zero z -velocity in the z -faces, i.e., slipping conditions. We weakly impose the displacement velocity $\nabla \phi^n$ with Nistche's method on the geometry $\mathcal{B}(t)$. The initial geometry \mathcal{B}_0 is mapped by $\mathbf{D} = \mathbf{D}_s \circ \phi_t$,

$$\mathbf{D}_s(\mathbf{x}, t) = \mathbf{x}_0 + \mathbf{R}(t) \cdot (\mathbf{x} - \mathbf{x}_0) + \mathbf{A}_x \sin(\omega_x t),$$

where $\mathbf{R}(t)$ is the rotation matrix with angular velocity $\omega = \pi/2$ rad/s, \mathbf{x}_0 is the center of the mesh, $\mathbf{A}_x = (0, 0.2)$ and $\omega_x = \pi/2$. The time map is defined as, $\phi_t(\mathbf{x}, t) = (\mathbf{x}, \phi_t(t))$,

$$\phi_t = \begin{cases} \left(\frac{t_a}{\gamma} \left(\frac{t}{t_a}\right)^\gamma\right) & \text{if } t < t_a, \\ (t - t_a) + \frac{t_a}{\gamma} & \text{otherwise.} \end{cases}$$

We set $\gamma = 2$ and $t_a = 1/8$. With this time map, the initial velocity of the geometry is zero.

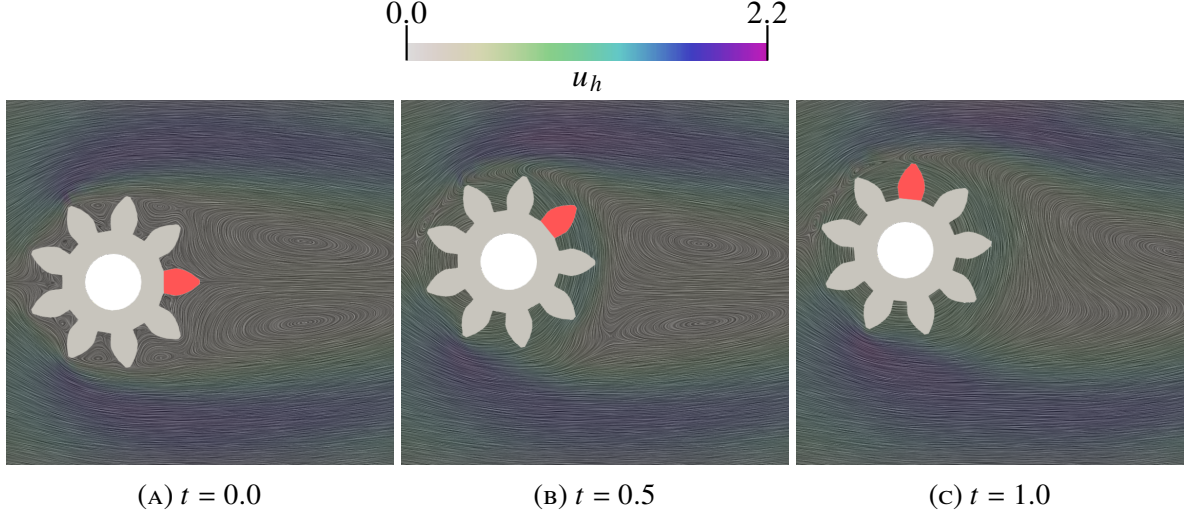


FIGURE 10. Representation of the line integral convolution (LIC) filter of the fluid simulation around an evolving geometry in Fig. 8 at $Re = 10^2$. The time step size is $\tau = 1/60$. The geometry combines rotation and displacements. The red tooth serves as a reference for visualizing the rotation.

In the 3D experiment of Fig. 9 and Fig. 11, we simulate a viscous flow ($Re \sim 0$) with the same boundary conditions as in the 2D experiment. However, we define a different inlet profile,

$$u(\mathbf{x}) = U_{\max}(4x_2 - 4x_2^2)(4x_3 - 4x_3^2),$$

that utilizes the 3D domain. The differences in the z -direction are clearly shown in Fig. 11. Equally, the z -faces have a slipping condition to hold the rotation of the wing in the z -direction. The initial geometry \mathcal{B}^0 is mapped by

$$\mathbf{D}(\mathbf{x}, t) = \mathbf{x}_0 + \mathbf{R}_\theta(t)(\mathbf{x} - \mathbf{x}_0),$$

where \mathbf{x}_0 is the center of the mesh and \mathbf{R}_θ is the rotation matrix of the angle $\theta(t) = \theta_{\max} \sin(\omega_\theta t)$ over the z -axis. Here, $\theta_{\max} = \pi/10$ and $\omega_\theta = \pi$. The 3D experiment is initialized with a non-zero velocity of the geometry.

We slightly optimize the number of time slab transfer operations in these experiments. Above a deformation threshold, e.g., $\max(\nabla \phi^n) < 0.8$, we maintain the spatial active mesh $\tilde{\mathcal{T}}^n$ between time slabs. In these cases, the initial value evaluation does not require mesh intersections, reducing computational cost.

6. CONCLUSIONS AND FUTURE WORK

In this work, we have introduced a novel space-time formulation for problems on moving domains with large displacements. The continuous problem at each time slab is pulled back to a constant-in-time domain (obtained by extrusion in time of the initial geometry). The resulting problem is discretized using unfitted FEM. Intersection algorithms between the boundary of the initial geometry and background mesh are used to compute the required integrals in the formulation. This way, we eliminate the requirement for four-dimensional geometric algorithms.

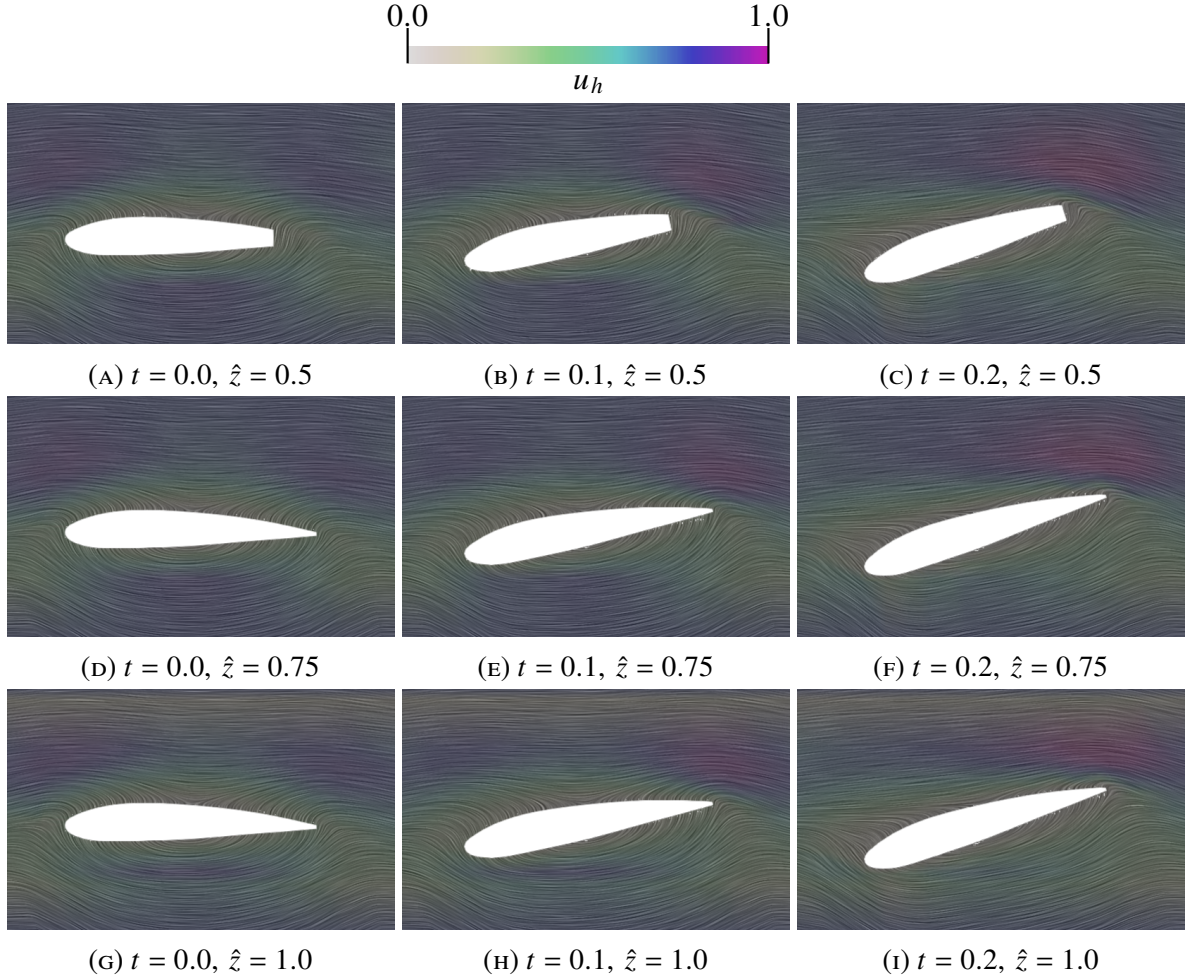


FIGURE 11. Representation of the LIC filter of the viscous flow around Fig. 9. The matrix representation shows several time slabs on different slices. Here, $\hat{z} = (z - z_0)/L_z$ represents the relative position in z where z_0 is the lower the z -coordinate and L_z the z -length. The step size of the simulation is $\tau = 1/120$. Note that the wing is not an extrusion of an airfoil. The central section ($\hat{z} = 0.5$) has a flat trailing edge (see Fig. 9).

The time discretization relies on DG schemes; the jump terms across time slabs are exactly integrated by computing the intersection of the reference and push-forward background meshes.

We have validated this method through an hp -convergence analysis of a manufactured solution using AgFEM. We have observed optimal convergence rates for two-dimensional and three-dimensional space domains in these experiments. The convergence has been validated by comparing it with another space-time analysis for unfitted FEM [30]. Additionally, we have observed the expected scaling of the condition number of the mass and stiffness matrices. Furthermore, we have demonstrated the practical applications of this methodology to the simulation of incompressible flows around rotating geometries in two examples, one with a two-dimensional geometry and another with a three-dimensional geometry.

Future work involves the numerical analysis of the method in the case in which the deformation maps do not much the boundary displacement by designing a high-order extension of the work in [32] and the extension of this method to distributed memory machines [44]. The geometrical component of this extension will be highly scalable, given that the presented algorithms are defined cell-wise and thus embarrassingly parallel, as they are in [12]. Distributed computations combined with background mesh refinement, e.g., using octree meshes, will allow

us to solve larger real-world applications. Additional developments include applying this method to FSI simulations. This extension will develop the full potential of the method in dynamic interface-coupling multiphysics simulations.

ACKNOWLEDGMENTS

This research was partially funded by the Australian Government through the Australian Research Council (project numbers DP210103092 and DP220103160). We acknowledge Grant PID2021-123611OB-I00 funded by MCIN/AEI/10.13039/501100011033 and by ERDF “A way of making Europe”. P. A. Martorell acknowledges the support received from Universitat Politècnica de Catalunya and Santander Bank through an FPI fellowship (FPI-UPC 2019). This work was also supported by computational resources provided by the Australian Government through NCI under the National Computational Merit Allocation Scheme.

REFERENCES

- [1] G. Karypis, K. Schloegel, and V. Kumar. ParMETIS: Parallel graph partitioning and sparse matrix ordering library. Technical report, Department of Computer Science and Engineering, University of Minnesota, 1997.
- [2] C. Burstedde, L. C. Wilcox, and O. Ghattas. p4est: Scalable algorithms for parallel adaptive mesh refinement on forests of octrees. *SIAM Journal on Scientific Computing*, 33(3): 1103–1133, Jan. 2011. doi:[10.1137/100791634](https://doi.org/10.1137/100791634).
- [3] C. Burstedde and J. Holke. A tetrahedral space-filling curve for nonconforming adaptive meshes. *SIAM Journal on Scientific Computing*, 38(5):C471–C503, Jan. 2016. doi:[10.1137/15m1040049](https://doi.org/10.1137/15m1040049).
- [4] E. Burman and M. A. Fernández. An unfitted nitsche method for incompressible fluid–structure interaction using overlapping meshes. *Computer Methods in Applied Mechanics and Engineering*, 279:497–514, sep 2014. doi:[10.1016/j.cma.2014.07.007](https://doi.org/10.1016/j.cma.2014.07.007).
- [5] L. Formaggia, F. Gatti, and S. Zonca. An XFEM/DG approach for fluid-structure interaction problems with contact. *Applications of Mathematics*, 66(2):183–211, jan 2021. doi:[10.21136/am.2021.0310-19](https://doi.org/10.21136/am.2021.0310-19).
- [6] B. Schott, C. Ager, and W. A. Wall. Monolithic cut finite element–based approaches for fluid-structure interaction. *International Journal for Numerical Methods in Engineering*, 119(8):757–796, apr 2019. doi:[10.1002/nme.6072](https://doi.org/10.1002/nme.6072).
- [7] R. Dekker, F. Meer, J. Maljaars, and L. Sluys. A cohesive XFEM model for simulating fatigue crack growth under mixed-mode loading and overloading. *International Journal for Numerical Methods in Engineering*, 118(10):561–577, feb 2019. doi:[10.1002/nme.6026](https://doi.org/10.1002/nme.6026).
- [8] B. Giovanardi, L. Formaggia, A. Scotti, and P. Zunino. Unfitted FEM for modelling the interaction of multiple fractures in a poroelastic medium. In *Lecture Notes in Computational Science and Engineering*, pages 331–352. Springer International Publishing, 2017. doi:[10.1007/978-3-319-71431-8_11](https://doi.org/10.1007/978-3-319-71431-8_11).
- [9] M. Carraturo, J. Jomo, S. Kollmannsberger, A. Reali, F. Auricchio, and E. Rank. Modeling and experimental validation of an immersed thermo-mechanical part-scale analysis for laser powder bed fusion processes. *Additive Manufacturing*, 36:101498, dec 2020. doi:[10.1016/j.addma.2020.101498](https://doi.org/10.1016/j.addma.2020.101498).
- [10] E. Neiva, M. Chiumenti, M. Cervera, E. Salsi, G. Piscopo, S. Badia, A. F. Martín, Z. Chen, C. Lee, and C. Davies. Numerical modelling of heat transfer and experimental validation in powder-bed fusion with the virtual domain approximation. *Finite Elements in Analysis and Design*, 168:103343, jan 2020. doi:[10.1016/j.finel.2019.103343](https://doi.org/10.1016/j.finel.2019.103343).
- [11] S. Badia, J. Hampton, and J. Principe. Embedded multilevel Monte Carlo for uncertainty quantification in random domains. *International Journal for Uncertainty Quantification*, 11(1):119–142, 2021. doi:[10.1615/int.j.uncertaintyquantification.2021032984](https://doi.org/10.1615/int.j.uncertaintyquantification.2021032984).

- [12] S. Badia, P. A. Martorell, and F. Verdugo. Geometrical discretisations for unfitted finite elements on explicit boundary representations. *Journal of Computational Physics*, 460: 111162, jul 2022. doi:[10.1016/j.jcp.2022.111162](https://doi.org/10.1016/j.jcp.2022.111162).
- [13] P. A. Martorell and S. Badia. High order unfitted finite element discretizations for explicit boundary representations. *arXiv*, 2023. doi:[10.48550/arXiv.2311.14363](https://doi.org/10.48550/arXiv.2311.14363).
- [14] F. de Prenter, C. Verhoosel, G. van Zwieten, and E. van Brummelen. Condition number analysis and preconditioning of the finite cell method. *Computer Methods in Applied Mechanics and Engineering*, 316:297–327, apr 2017. doi:[10.1016/j.cma.2016.07.006](https://doi.org/10.1016/j.cma.2016.07.006).
- [15] E. Burman. Ghost penalty. *Comptes Rendus Mathématique*, 348(21-22):1217–1220, nov 2010. doi:[10.1016/j.crma.2010.10.006](https://doi.org/10.1016/j.crma.2010.10.006).
- [16] E. Burman, S. Claus, P. Hansbo, M. G. Larson, and A. Massing. CutFEM: Discretizing geometry and partial differential equations. *International Journal for Numerical Methods in Engineering*, 104(7):472–501, dec 2014. doi:[10.1002/nme.4823](https://doi.org/10.1002/nme.4823).
- [17] B. Müller, S. Krämer-Eis, F. Kummer, and M. Oberlack. A high-order discontinuous galerkin method for compressible flows with immersed boundaries. *International Journal for Numerical Methods in Engineering*, 110(1):3–30, nov 2016. doi:[10.1002/nme.5343](https://doi.org/10.1002/nme.5343).
- [18] S. Badia, F. Verdugo, and A. F. Martín. The aggregated unfitted finite element method for elliptic problems. *Computer Methods in Applied Mechanics and Engineering*, 336:533–553, jul 2018. doi:[10.1016/j.cma.2018.03.022](https://doi.org/10.1016/j.cma.2018.03.022).
- [19] S. Badia, A. F. Martín, and F. Verdugo. Mixed aggregated finite element methods for the unfitted discretization of the stokes problem. *SIAM Journal on Scientific Computing*, 40(6): B1541–B1576, jan 2018. doi:[10.1137/18m1185624](https://doi.org/10.1137/18m1185624).
- [20] F. Verdugo, A. F. Martín, and S. Badia. Distributed-memory parallelization of the aggregated unfitted finite element method. *Computer Methods in Applied Mechanics and Engineering*, 357:112583, dec 2019. doi:[10.1016/j.cma.2019.112583](https://doi.org/10.1016/j.cma.2019.112583).
- [21] S. Badia, A. F. Martín, E. Neiva, and F. Verdugo. The aggregated unfitted finite element method on parallel tree-based adaptive meshes. *SIAM Journal on Scientific Computing*, 43 (3):C203–C234, jan 2021. doi:[10.1137/20m1344512](https://doi.org/10.1137/20m1344512).
- [22] E. Neiva and S. Badia. Robust and scalable h-adaptive aggregated unfitted finite elements for interface elliptic problems. *Computer Methods in Applied Mechanics and Engineering*, 380:113769, jul 2021. doi:[10.1016/j.cma.2021.113769](https://doi.org/10.1016/j.cma.2021.113769).
- [23] S. Badia, E. Neiva, and F. Verdugo. Robust high-order unfitted finite elements by interpolation-based discrete extension. *Computers & Mathematics with Applications*, 127:105–126, dec 2022. doi:[10.1016/j.camwa.2022.09.027](https://doi.org/10.1016/j.camwa.2022.09.027).
- [24] S. Badia, E. Neiva, and F. Verdugo. Linking ghost penalty and aggregated unfitted methods. *Computer Methods in Applied Mechanics and Engineering*, 388:114232, jan 2022. doi:[10.1016/j.cma.2021.114232](https://doi.org/10.1016/j.cma.2021.114232).
- [25] G. L. Beau, S. Ray, S. Aliabadi, and T. Tezduyar. SUPG finite element computation of compressible flows with the entropy and conservation variables formulations. *Computer Methods in Applied Mechanics and Engineering*, 104(3):397–422, may 1993. doi:[10.1016/0045-7825\(93\)90033-t](https://doi.org/10.1016/0045-7825(93)90033-t).
- [26] T. E. Tezduyar, S. Sathe, R. Keedy, and K. Stein. Space-time finite element techniques for computation of fluid-structure interactions. *Computer Methods in Applied Mechanics and Engineering*, 195(17-18):2002–2027, mar 2006. doi:[10.1016/j.cma.2004.09.014](https://doi.org/10.1016/j.cma.2004.09.014).
- [27] L. L. Thompson and P. M. Pinsky. A space-time finite element method for structural acoustics in infinite domains part 1: Formulation, stability and convergence. *Computer Methods in Applied Mechanics and Engineering*, 132(3-4):195–227, jun 1996. doi:[10.1016/0045-7825\(95\)00955-8](https://doi.org/10.1016/0045-7825(95)00955-8).
- [28] J. Donea, S. Giuliani, and J. Halleux. An arbitrary lagrangian-eulerian finite element method for transient dynamic fluid-structure interactions. *Computer Methods in Applied Mechanics*

- and Engineering*, 33(1-3):689–723, sep 1982. doi:[10.1016/0045-7825\(82\)90128-1](https://doi.org/10.1016/0045-7825(82)90128-1).
- [29] F. Nobile and L. Formaggia. A stability analysis for the arbitrary lagrangian eulerian formulation with finite elements. *East-West Journal of Numerical Mathematics*, 7(2): 105–132, 1999.
 - [30] S. Badia, H. Dilip, and F. Verdugo. Space-time unfitted finite element methods for time-dependent problems on moving domains. *Computers & Mathematics with Applications*, 135:60–76, apr 2023. doi:[10.1016/j.camwa.2023.01.032](https://doi.org/10.1016/j.camwa.2023.01.032).
 - [31] F. Heimann, C. Lehrenfeld, and J. Preuß. Geometrically higher order unfitted space-time methods for pdes on moving domains. *SIAM Journal on Scientific Computing*, 45(2): B139–B165, Mar. 2023. doi:[10.1137/22m1476034](https://doi.org/10.1137/22m1476034).
 - [32] C. Lehrenfeld and M. Olshanskii. An eulerian finite element method for pdes in time-dependent domains. *ESAIM: Mathematical Modelling and Numerical Analysis*, 53(2): 585–614, Mar. 2019. doi:[10.1051/m2an/2018068](https://doi.org/10.1051/m2an/2018068).
 - [33] F. de Prenter, C. V. Verhoosel, E. H. van Brummelen, M. G. Larson, and S. Badia. Stability and conditioning of immersed finite element methods: Analysis and remedies. *Archives of Computational Methods in Engineering*, 30(6):3617–3656, May 2023. doi:[10.1007/s11831-023-09913-0](https://doi.org/10.1007/s11831-023-09913-0).
 - [34] J. Nitsche. Über ein variationsprinzip zur lösung von dirichlet-problemen bei verwendung von teilräumen, die keinen randbedingungen unterworfen sind. *Abhandlungen aus dem Mathematischen Seminar der Universität Hamburg*, 36(1):9–15, July 1971. doi:[10.1007/bf02995904](https://doi.org/10.1007/bf02995904).
 - [35] F. Heimann and C. Lehrenfeld. Geometrically higher order unfitted space-time methods for pdes on moving domains: Geometry error analysis. *arXiv*, 2023. doi:[10.48550/arXiv.2311.02348](https://doi.org/10.48550/arXiv.2311.02348).
 - [36] J. Bonet and R. D. Wood. *Nonlinear continuum mechanics for finite element analysis*. Cambridge university press, 1997.
 - [37] K. Sugihara. A robust and consistent algorithm for intersecting convex polyhedra. *Computer Graphics Forum*, 13(3):45–54, aug 1994. doi:[10.1111/1467-8659.1330045](https://doi.org/10.1111/1467-8659.1330045).
 - [38] J. Bezanson, A. Edelman, S. Karpinski, and V. B. Shah. Julia: A fresh approach to numerical computing. *SIAM Review*, 59(1):65–98, jan 2017. doi:[10.1137/141000671](https://doi.org/10.1137/141000671).
 - [39] F. Verdugo and S. Badia. The software design of gridap: A finite element package based on the julia JIT compiler. *Computer Physics Communications*, 276:108341, jul 2022. doi:[10.1016/j.cpc.2022.108341](https://doi.org/10.1016/j.cpc.2022.108341).
 - [40] F. Verdugo, E. Neiva, and S. Badia. GridapEmbedded. Version 0.8., Jan. 2023. Available at <https://github.com/gridap/GridapEmbedded.jl>.
 - [41] P. A. Martorell, S. Badia, and F. Verdugo. STLCutters. *Zenodo*, Sept. 2021. doi:[10.5281/zenodo.5444427](https://doi.org/10.5281/zenodo.5444427).
 - [42] I. Smears. Robust and efficient preconditioners for the discontinuous galerkin time-stepping method. *IMA Journal of Numerical Analysis*, page drw050, oct 2016. doi:[10.1093/imanum/drw050](https://doi.org/10.1093/imanum/drw050).
 - [43] Q. Zhou and A. Jacobson. Thingi10K: A Dataset of 10,000 3D-Printing Models. *arXiv*, 2016. doi:[10.48550/arXiv.1605.04797](https://doi.org/10.48550/arXiv.1605.04797).
 - [44] S. Badia, A. F. Martín, and F. Verdugo. GridapDistributed: a massively parallel finite element toolbox in julia. *Journal of Open Source Software*, 7(74):4157, jun 2022. doi:[10.21105/joss.04157](https://doi.org/10.21105/joss.04157).